Special Topics

Hyper-Ordered Structures: Recent Progress and Future Perspectives

Structure Determination in a New Class of Amorphous Cluster Compounds with Extreme Nonlinear Optical Properties

Wolf-Christian Pilgrim[1]*, Jens Rüdiger Stellhorn[4,1], Benjamin Danilo Klee[1],
Jonathan Link Vasco[1], Benedict Paulus[1], Anita Zeidler[2],
Shinya Hosokawa[3,1], Shinjiro Hayakawa[4], and Stefanie Dehnen[1]

[1]Department of Chemistry, Philipps-Univ. of Marburg, 35032 Marburg, Germany
[2]Department of Physics, University of Bath, Bath, BA2 7AY, U.K.
[3]Institute of Industrial Nanomaterials, Kumamoto University, Kumamoto 860-8555, Japan
[4]Department of Applied Chemistry, Hiroshima University, Higashihiroshima, Hiroshima 739-8527, Japan

The microscopic structure of two new infrared-driven amorphous white light generators, namely $[(PhSn)_4S_6]$ and $[(CpSn)_4S_6]$ and a related amorphous material $[(NpSn)_4S_6]$, showing 2nd harmonics generation instead, were explored by X-ray and neutron diffraction, EXAFS and Reverse Monte Carlo simulations to explore relations between their extreme nonlinear optical behavior and microscopic structural properties. The current state of research is reported and experimental and simulation results are discussed. The prominent observation is that the molecular units are distorted in the WLG materials which seems not to be the case for the 2nd harmonics generator. Associated is the formation of a net of similarly spaced intra- and intermolecular sulfur atoms which is interpreted as a vibrational network that could explain the high receptivity of the material for infrared radiation. It is also found that the molecules arrange in chains with staggered configuration regarding the arrangement of the organic ligands.

1. Introduction

For the far longer time of human history, light was produced in form of burning objects, like torches and oil lamps. These illuminants emitted an electromagnetic spectrum fully comprising the part visible to humans. The invention of the light bulb was only made 150 years ago, and yet it was the first decisive breakthrough in the development of light generation. However, the underlying process was still based on hot glowing objects. Hence, it was still rather unfavorable in terms of energy efficiency, since the larger ranges of the emitted spectra were still located in the red and infrared regimes, and most of the energy dissipated as heat. After all, incandescent lamps with filaments heated up to about 3000 K have an intensity maximum which is already in the visible range, nevertheless, the infrared portion is still about 40–50%. Numerous attempts were therefore undertaken during the 20th century until today to develop new and more efficient light generation techniques. The most promising result of these efforts is probably the Light–Emitting–Diode (LED).[1] In terms of energy efficiency, this technology represents a real quantum leap in the development of light sources. Normally, such devices consist of inorganic semiconductors and their spectra are located in the near ultra-violet. Luminophores and phosphors are therefore used to convert this radiation into an optically suitable frequency distribution in the visible regime.[2–5] The organic LED is a similar concept based on organic semiconductors where the band gap and hence the emitted spectrum can be tuned by chemical modifications on the molecular level. Red, green, and blue devices are then usually combined to also provide warm white optical emission.[6–9] LEDs are advantageous for many daily applications and one important feature is that the radiation pattern is usually less oriented allowing their use in, e.g., displays where high viewing angles are preferred. However, for other applications a high directional emission of spectra in the visible range is often desired. In fact, the research for "Laser-like" White Light Generators (WLG)

goes back to the nineteen seventies and resulted in so called Super–Continuum–Generators (SCG) where use is made of non-linear optical (NLO) effects in different materials.[10,11] The white light radiation of these SCGs is point-like, sustaining the beam characteristics of the short-pulsed high energy pumping laser, which are needed to provide the high field strengths necessary to invoke the higher order NLO effects. Common materials used here are YAG, Sapphire, CaF_2-crystals, optical fibers and waveguide-based sources. However, the problem with such techniques is that the required experimental installations are bulky and expensive, restricting the use of these devices to pure scientific or medical applications. Recently, a group of relatively simple chemical compounds was reported to exhibit extreme non-linear optical behavior when irradiated by an unpretentious, inexpensive continuous wave near infrared (CW-NIR) laser diode.[12,13] Also, these materials are comparatively easily and efficiently to synthesize. The development of such products into materials that can be used in applications is hence of great interest and could open up the way for a wide range of new and low-cost optical devices. They are prepared as powdered solids and emit either second-harmonics or warm white optical spectra which retain the high-directional beam characteristics of the driving laser. Their molecular building blocks are organic-inorganic hybrid-compounds consisting of cluster-like molecules with general formula $[(RX)_4Y_6]$, where X is a group-14 element, Y is a chalcogen and R represents an organic ligand attached to the group 14 atom. The inorganic constituents X and Y form an adamantane-like cage, and the organic substituents R protect the inorganic cluster cores from further reaction to more stable compounds. The resulting general shape of these clusters is displayed in Fig. 1, where the organotin sulfide cluster $[(PhSn)_4S_6]$ is shown, with phenyl ligands (Ph = $-C_6H_5$) attached to the tin atoms of the adamantane shaped Sn–S cluster core. Variation of the ligands and/or the chalcogens or of the group 14 element allows great chemical variability of the cluster compositions. Table I outlines some of the compounds

©2022 The Author(s)
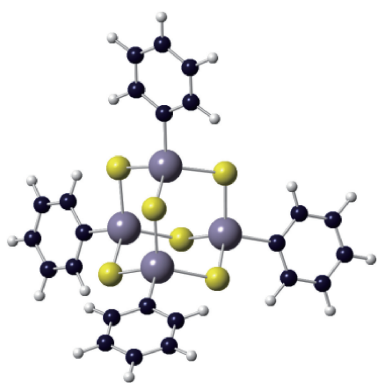
Fig. 1. (Color online) Representation of the [(PhSn)$_4$S$_6$] cluster (**1**), one of the amorphous white light generators. Organic phenyl ligands are attached to the Sn atoms of the tins-sulfur cluster core.

Table I. Adamantane-like inorganic/organic adamantane-based compounds yet investigated and their non-linear optical response to CW-NIR laser irradiation (a = amorphous, c = crystalline).

Compound	Morphology	Optical response	Organic Ligand
[(StySn)$_4$S$_6$][12]	a	WLG	styryl
[(PhSn)$_4$S$_6$][13](**1**)	a	WLG	phenyl
[(CpSn)$_4$S$_6$][14](**2**)	a	WLG	cyclopentadienyl
[(NpSn)$_4$S$_6$][13](**3**)	a	SHG	naphtyl
[(MeSn)$_4$S$_6$][13]	a	SHG	methyl
[(BnSn)$_4$S$_6$][14]	c	SHG	benzyl
[(R^{1}Sn)$_4$S$_6$][14]	a	WLG	(CH$_2$)$_2$(C$_6$H$_4$)CO$_2$Et
[(CySn)$_4$S$_6$][14]	a	WLG	cyclohexanyl
[(PhSn)$_4$Se$_6$][15]	a	WLG	phenyl
[(BnSn)$_4$Se$_6$][14]	c	SHG	benzyl
[(R^{1}Sn)$_4$Se$_6$][14]	a	WLG	(CH$_2$)$_2$(C$_6$H$_4$)CO$_2$Et
[(CpSn)$_4$Se$_6$][14]	a	WLG	cyclopentadienyl
[(CySn)$_4$Se$_6$][14]	a	WLG	cyclohexanyl
[(PhGe)$_4$S$_6$][13]	a	WLG	phenyl
[(PhSi)$_4$S$_6$][16](**4**)	c	SHG	phenyl

synthesized so far together with their respective optical responses. All of these materials show strong NLO-reactions either as SHG or WLG. However, while the crystalline compounds clearly react as second harmonics generators, the amorphous materials prefer to emit white spectra, indicating that disorder seems to be a mandatory requirement for WLG. The influence of morphology is exemplary demonstrated for the two systems (**1**) and (**4**) of Table I in Fig. 2. The two compounds differ only by the exchange of Sn by Si in the cluster core, but they show completely different optical and morphological properties. The Figure depicts their optical answers when being irradiated by a 980 nm laser-line (1.265 eV). While the Si-based compound replies with a distinct 2nd order harmonics at 2.53 eV, the Sn-containing material responds with a broad white spectrum ranging from about 1.5 to 3 eV. Also shown in the Figure are the respective diffraction-pattern of the two substances. The [(PhSi)$_4$S$_6$] material (**4**) is clearly crystalline, as indicated by the Bragg peak dominated diffraction pattern, while [(PhSn)$_4$S$_6$], (**1**), is fully amorphous and the scattered X-rays yield a structure factor $S(Q)$, typical of a fully disordered system. Although both clusters are similarly shaped and differ only by one single atom type in the cluster-core, the structural morphology is vastly different, as are the optical responses. The fact
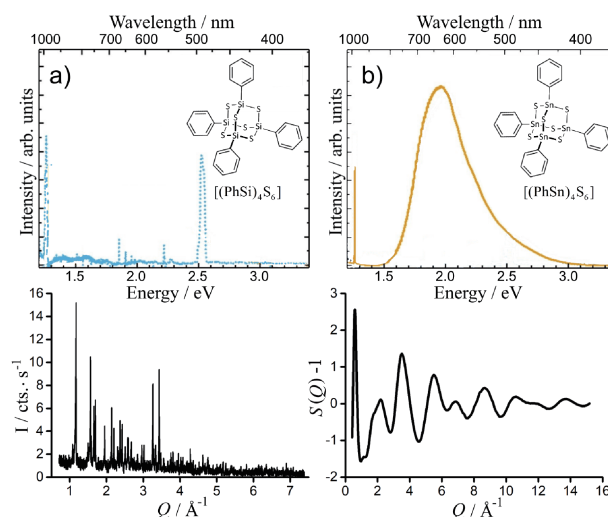
Fig. 2. (Color online) NLO-responses from (a) the crystalline and (b) the amorphous materials, (**1**) and (**4**), respectively (top). The driving excitation is visible at 1.265 eV in each spectrum. The 2nd-harmonic of (a) is clearly seen at 2.53 eV, while (b) depicts a broad WLG. The respective X-ray patterns are also shown below indicating that the SHG-material is clearly crystalline (left) while the WLG material (right) shows the typical structure factor $S(Q)$ of an amorphous solid.

that WLG is obviously never observed from crystalline cluster materials indicates that the effect is enabled by certain microscopic structural correlations or degrees of freedom that are only possible in a sufficiently disordered state. The amorphous materials (**1**) and (**2**) were clearly identified as WLGs, while (**3**), although also not crystalline, does not emit a white spectrum upon irradiation but clearly reacts as a SHG. We therefore explored all three cluster materials with respect to their microscopic structure to determine whether one can identify characteristic structural differences in the interatomic and intermolecular range between the amorphous SHG (**3**) and the two amorphous WLGs materials (**1**) and (**2**). Here, we will give a short report on the current status of our work.

2. Background of Experimental Methods and Data Analysis

2.1 X-ray and neutron scattering

While crystal structure analysis is nowadays a standard technique in chemistry and physics, the detailed determination of structural relationships in disordered matter is still a major and demanding challenge, although diffraction studies on disordered matter are almost as old[17,18] as von Laue's first experiments of X-ray diffraction from crystal lattices in 1912.[19] Various excellent review articles on this topic exist (see, e.g., Refs. 20 and 21), so we will just give a very brief outline here. In the simplest case, the total structure factor $S(Q)$ as the central function, is directly obtained from the pure scattering intensity $I(Q)$ either using X-rays or neutrons. It is the total interference function of the sample and can be interpreted as the distribution of interatomic pair distances in reciprocal space. $S(Q)$ is related to the pair distribution function (PDF), $g(r)$ via Fourier-transform representing the same statistical relations in real space. Its values are proportional to finding an atom at position r when there is a reference atom located at the origin, averaged over the whole ensemble of atoms in the irradiated part of the sample.

Average coordination numbers and interatomic distances can generally be derived from the PDF and this is in fact a straight forward task when simple systems such as mona-tomic glasses or liquids are being explored. However, this is no longer the case if the sample contains more than one chemical component, e.g., when complex alloys, amorphous semiconductors and metals or other technically interesting systems are being investigated. Then, the interpretation of $g(r)$ or $S(Q)$ is no longer unambiguous, since various arrangements of different atoms may lead to similar functions. The goal of structural investigations on compli-cated materials using scattering techniques is therefore always to overcome this ambiguity of the total structure factor $S(Q)$ in order to obtain unmistakable, reliable structural information. Since $S(Q)$ is basically defined as a sum of scattering contributions from pairs of atoms,[20,21] it is possible to also decompose it into the sum of partial structure factors $S_{ij}(Q)$, where i and j run over all combinations of two chemical species,[22]

$$S(Q) = \sum_{i,j} w_{i,j} \cdot S_{i,j}(Q). \qquad (1)$$

For a system consisting of n chemical components, $n(n + 1)/2$ different $S_{ij}(Q)$ exist. The partial structure factors represent the structural correlations between particles of chemical species i to particles of species j in reciprocal space and the partial pair distribution functions (PPDF) $g_{ij}(r)$, obtained from Fourier-transforming the $S_{ij}(Q)$, determine the probability of finding a particle of species j at position r, if there is particle of species i at the origin. Their determination is the goal in any structure exploration on disordered materials consisting of more than one chemical component. These functions can readily be interpreted and they contain the required information to comprehend the correlations between the particles, which is the key for an understanding of the structural arrangement of atoms in disordered matter. The w_{ij} in Eq. (1) represent the weighting factors of the individual $S_{ij}(Q)$. They are determined by the respective concentrations and scattering lengths of each component and are defined as

$$w_{ij} = \frac{x_i x_j f_i f_j}{\langle f \rangle^2}. \qquad (2)$$

x_i and f_i in Eq. (2) denote the respective portion and scattering length of component i, respectively and the denominator determines the square of the concentration-averaged scattering length of the sample [either X-ray formfactor $f(Q)$ or neutron scattering length b]. The problem is, that the $S_{ij}(Q)$ functions of Eq. (1) are a priori not known and cannot directly be obtained from a single measurement of the total $S(Q)$. For a direct determination of the $n(n + 1)/2$ unknown $S_{ij}(Q)$ functions an equally number of linear equations would be needed to form a linear set of inhomogeneous equations which could then in principle be solved. However, for this, $n(n + 1)/2$ different $S(Q)$ measurements of the same sample are needed, yielding $n(n + 1)/2$ different scattering patterns, without changing the chemical composition, which is a difficult to impossible task. However, for not too complex compositions such techniques exist as, e.g., neutron diffraction with isotopic substitution (NDIS)[20] or anomalous X-ray scattering (AXS).[23,24] In the latter case, the full set of required equations is usually not obtained, and even then, the contrast between these functions is usually too small to numerically solve the resulting system of equations in a satisfactory way.[20,21] Therefore, AXS data analysis is typically combined with Reverse Monte Carlo (RMC) simulations.[25,26] However, both NDIS and AXS are sophisticated and difficult methods, and a high level of experience is required to reliably perform the associated data analyses.

Another kind of challenge exists when the elementary building blocks of an amorphous sample consist of molecules. This situation is also widely discussed in the literature, and a number of intriguing review articles exists here as well (see, e.g., Ref. 27). Again, since $S(Q)$ is defined as the sum of the scattering from pairs of atoms, the total structure factor, after appropriate rearrangement, can also be written as a sum of two contributions representing the intra- and intermolecular correlation respectively, and is then simply defined as,

$$S(Q) = f_1(Q) + D_m(Q). \qquad (3)$$

Here, $f_1(Q)$ is denoted the molecular formfactor.[27] It represents the contribution to $S(Q)$ that originates solely from atom–atom spacings within the molecular entities. Here, we will define it as

$$f_1(Q) = \frac{1}{\left(\sum_i f_i \right)^2} \sum_{i,j} f_i \cdot f_j \cdot \frac{\sin(Q \cdot r_{ij})}{Q \cdot r_{ij}}. \qquad (4)$$

The i, j run over all combination of atom pairs within the molecule. $D_m(Q)$ in Eq. (3) denotes the scattering from atom pairs belonging to different molecules, it hence represents the intermolecular contribution to $S(Q)$. It depends on the mutual spatial orientation of the molecules and is therefore characteristic of the intermolecular interactions. If the molecular structure is known $f_1(Q)$ can be computed and $D_m(Q)$ is determined by the difference between $S(Q)$ and $f_1(Q)$. However, the interpretation of the intermolecular contribution is a sophisticated task and a direct translation into real space is difficult. Therefore, the analysis of scattering laws obtained from molecular systems should also be supported by additional methods such as computer simulations. We will therefore briefly discuss the use of RMC simulation for the exploration of disordered molecular systems.

2.2 Molecular RMC simulation

In standard RMC simulations, computer generated hard-sphere atoms of identical composition as a real sample are iteratively moved inside a simulation box with periodic-boundary conditions and a scattering law $S(Q)_{calc}$ is computed after each step until it matches the experimental $S(Q)$. Individual partial pair correlation functions are then obtained from the virtual ensemble which gives further insight into the specific microscopic arrangements of the real material.[28] The problem of RMC however is, that the simulated $S(Q)$ for a multi component system will not be unique,[29] as was already mentioned above. Therefore, strong simulation constraints are required to enforce unambiguous simulation results. Beneath hard constraints like minimum atomic distances for the different atomic sizes, so called cut-off-limits, additional scattering laws of the same sample as, e.g., additional X-ray and neutron scattering data may be

used as further constraints, e.g., from AXS[20,21,30)] or from NDIS.[20,31,32)] The situation is however different for molecular substances, where complete well-defined molecular units are moved in a single step instead of single atoms, and the molecular structure is preserved throughout the simulation. This is a strong constraint, and a molecular RMC (m-RMC) simulation carried out to match a total experimental $S(Q)$ will therefore provide a reliable simulation output. Such approaches were already performed in the past, they were however limited to small or symmetrically simple, rigid molecules ignoring internal degrees of freedom.[33,34)] The reason for this limitation is, that the implementation of m-RMC in common simulation software packages is difficult, and there are a number of problems to overcome. First, a reasonable molecular structure must be assumed beforehand. Internal degrees of freedom like rotations about bonds must be considered as well as possible molecular deformations in the condensed amorphous phase so as to only enable the simulation to change structural properties that are well reflected in the available data. A purely rigid molecular entity might not necessarily provide a meaningful structural model for a complex molecular system.[35)] The uncertainty of atomic positions due to thermal vibrations is also problematic. Typically, this is considered by a Debye–Waller approach, which, however, cannot account for the real vibrational volume and may lead to unrealistically high free volumes.[36)] It is also questionable whether an artificial isotropic broadening of the atom positions is realistic, or whether one should rather expect ellipsoid-like spatial distributions in the molecular case.

Because of all these difficulties of the rigid m-RMC-simulation, structural investigations on disordered molecular systems have more recently been combined with molecular dynamics (MD) based methods, such as combined MD/RMC or with Empirical Potential Structure Refinement simulations (EPSR).[37–39)] In our m-RMC simulation we have implemented the additional option to slightly and independently move intramolecular atoms in order to simulate corresponding molecular distortions or anisotropic vibrations.

2.3 EXAFS and XANES

A complementary view of the short-range structural features can be gained from X-ray spectroscopy methods performed in the vicinity of an X-ray absorption edge. Typically, two techniques are distinguished based on the energetic region that is probed: the first is X-Ray Absorption Near Edge Structure (XANES), probing the energy range "near the edge", conventionally within about 50 eV of the absorption edge. Beyond this region, Extended X-ray Absorption Fine Structure (EXAFS) spectroscopy can extend to more than 1000 eV above the edge. From a XANES experiment, also called Near Edge X-ray Absorption Fine Structure, we can obtain information on the local electronic properties as well as on structural features, i.e., chemical bonds as well as long- or intermediate-range interactions. The interpretation of a XANES spectrum can be rather challenging, however, and is effectively assisted by computer simulations, using, e.g., FEFF[40,41)] or FDMNES.[41)] EXAFS spectroscopy, on the other hand, is based on the oscillatory modulation of the X-ray absorption coefficient as a function of X-ray photon energy beyond an X-ray absorption edge,[42)]

and can provide one-dimensionally averaged, element-specific structural information, such as atomic distances and vibrations. Both methods are well developed and meanwhile belong to standard characterization techniques for investigations of atomic-scale properties. They are extremely versatile, and can be applied to ordered as well as disordered states of matter. Phenomenologically, the XAFS spectrum χ is defined as the normalized, oscillatory part of the X-ray absorption above a given absorption edge. The oscillations arise from an interference effect: the outgoing photoelectron that is excited from the incoming X-ray, typically from a low-lying K- or L-shell, will be scattered from neighboring atoms, and the amplitude of all the reflected electron waves at the position of the absorbing atom add either constructively or destructively to the outgoing photoelectron wave. The photoelectron wavevector is conventionally denoted k, in contrast to Q in X-ray scattering, and can be written as

$$k = \sqrt{\frac{2m_e}{\hbar^2}(E - E_0)}, \qquad (5)$$

where E_0 is the threshold energy of the absorption edge, and m_e is the mass of the electron. With this parameter, we can define the XAFS spectrum $\chi(k)$ as a sum of contributions from all neighboring atoms, or more generally, from all possible scattering paths j.[42)]

$$\chi(k) = \sum_j \frac{S_0^2 N_j f_j(k)}{kR_j^2} e^{-2R_j/\lambda(k)} e^{-2k^2\sigma_j^2} \sin(2kR_j + \delta_j(k)). \quad (6)$$

Here, R_j is the absorber-scatterer distance, S_0^2 is the so-called amplitude reduction factor (related to many-body effects), N_j is the coordination number of j, $f_j(k)$ is the backscattering amplitude from each neighboring atom, $\lambda(k)$ is the mean-free path of the photoelectron, σ_j is the variance in the absorber-scatterer distance (commonly interpreted as Debye–Waller factor), and $\delta(k)$ is the total phase shift experienced by the photoelectron. The factor due to the mean free path $\lambda(k)$ of the photoelectron (typically 5 to 30 Å) is largely responsible for the relatively short range probed by EXAFS, which is generally within the first or second coordination shell in amorphous compounds, and in the order of magnitude of 10 Å in crystals. It should also be noted that single scattering paths are dominating in the low R_j region, but multiple scattering effects quickly become important beyond the first coordination shell of an atom and lead to a veritable multitude of scattering paths j. It is readily seen that the structural information is contained in the parameters R_j, N_j, and σ_j. These can be fitted directly with available software like the DEMETER program package,[43)] but can also be determined by RMC modelling. The other parameters $f(k)$, $\delta(k)$, and $\lambda(k)$ are nowadays typically calculated from programs like FEFF[44)] and given as input into the structure refinement process. For the interpretation of EXAFS data, the Fourier transform magnitudes of the EXAFS spectra, $|FT(\chi(k))|$, are helpful. Similar to pair correlation functions obtained from Fourier transformed $S(Q)$s in X-ray scattering, these functions provide a handy illustration of the 1-D average real-space environment around the absorber atom. It is important to keep in mind, however, that these functions are not pair correlations in the strict sense. Most obviously, the EXAFS phase shift $\delta_j(k)$ typically leads to a shift of the real-space signal by some 0.1 Å. Additionally, the oscillatory

nature of the (complex valued) $\chi(k)$ functions frequently leads to signals with several peaks in $|FT(\chi(k))|$ but belonging to the same scattering path. For further reading and more detailed information on these techniques, we refer to the vast existing literature, e.g., regarding XANES[45] or EXAFS.[42,44,45]

3. Experiments and Computations

For the phenyl-tin-sulfur and cyclopentadienyl-tin-sulfur clusters, **(1)** and **(2)** in Table I, respectively, X ray scattering experiments were performed in transmission geometry at beamline P02.1[46] of the PETRA III storage ring of the Deutsches Elektronen-SYnchrotron (DESY) using a primary energy of 59.87 keV. The samples were confined in X-ray capillaries of 1 mm outer diameter and scattering data were collected using a flat pixel detector with pixel size of $200 \times 200\,\mu m^2$. The sample-detector distance was set to 240.18 mm. Raw data were processed using the software DAWN.[47] An in-house Bruker D5000 diffractometer, equipped with a Goebel mirror to optimize the primary beam from a Mo tube, was used to study a freshly prepared sample of the amorphous SHG material **(3)**, also contained in a 1 mm X-ray capillary for transmission measurements. An attempt to also obtain a decent $S(Q)$ for **(3)** from the PETRA III synchrotron source failed due to crystallization of the sample. All data were corrected for background- and air-scattering, self-absorption, polarization and Compton contribution and were then normalized to $S(Q)$. The X-ray $S(Q)$s of the inorganic cluster materials are dominated by scattering from the heavier atoms of the Sn–S cluster cores, whereas the organic ligands contribute only with small weighting factors. Therefore, an additional neutron scattering experiment was performed on **(2)** where a degree of deuteration of about 90% was accomplished to suppress the incoherent scattering from the hydrogen atoms. For neutrons, the scattering length of the D and C atoms are of similar magnitude as those for Sn and S. The experiment was performed on the D4C diffractometer at the Institute Laue–Langevin in Grenoble/France using an incident wavelength of 0.4957(1) Å. Patterns were measured for the sample in a vanadium can of 6.05 mm inner diameter and 0.15 mm wall thickness, the empty can, the empty instrument and a vanadium rod of 6.08 mm diameter for normalization purposes. The data were corrected for background scattering, attenuation, multiple scattering and inelastic scattering as is outlined in, e.g., Ref. 48. EXAFS spectra were obtained at the sulfur K- and L_3-edges and at the K-edge of the tin atoms. The Sn K-edge data were obtained at beamline P65, located at PETRA III (DESY) and the sulfur K- and tin L_3-edge data were measured at beamline BL-11 of the Hiroshima Synchrotron HiSOR in Japan. At BL-11, the measurements were carried out at room temperature and the sample was directly measured, sandwiched between two polypropylene foils. At P65 additional measurements at 34 K were carried out and the samples were mixed with graphite and pressed to pellets. The scans were performed in transmission mode with absorption lengths $\mu = 2.0$ (P65, DESY) and $\mu = 1.5$ (BL11, HiSOR). The data were analyzed using the DEMETER software package (Athena and Artemis).[43] EXAFS spectra were normalized and background was calculated using the AUTOBK algorithm. An m-RMC-analysis on **(1)** was performed, for which we have

manipulated an existing RMC simulation code based on the RMC_POT++ program,[49] which already offers the option to group atoms as a rigid molecule. We have generated a code enabling molecular translation and rotation, and also free rotation of the phenyl groups.[50] This code was then further optimized in terms of computational- and simulation speed.[51] During the simulation 216 molecules of the phenyl-based molecule **(1)** were moved in a cubic simulation box with 55.836 Å edge length. Two sets of simulations were carried out. In the first set, the molecules consisted of rigid copies of the DFT-calculated phenyl-cluster **(1)**. In the second simulation, the sulfur and tin atoms were allowed to slightly vary their coordinates within the cluster-core. The motion of chemically bonded atom pairs was thereby restricted within certain limits. The Sn–S bond, however, was left more or less unconstrained between 2.05 and 2.65 Å, since the weighting factors for both, X-ray and EXAFS data, are large for this correlation, providing sufficient information density for a reliable simulation. In contrast, the variability of the Sn–C bond was strongly constrained between 2.05 and 2.25 Å to compensate for the smaller weighting factor and thus the smaller information density in the data. The C atoms were not allowed to move intramolecularly. The attached Sn atoms thus always remained close to their original coordinates, which inevitably ensured an intact overall molecular structure during the simulation.
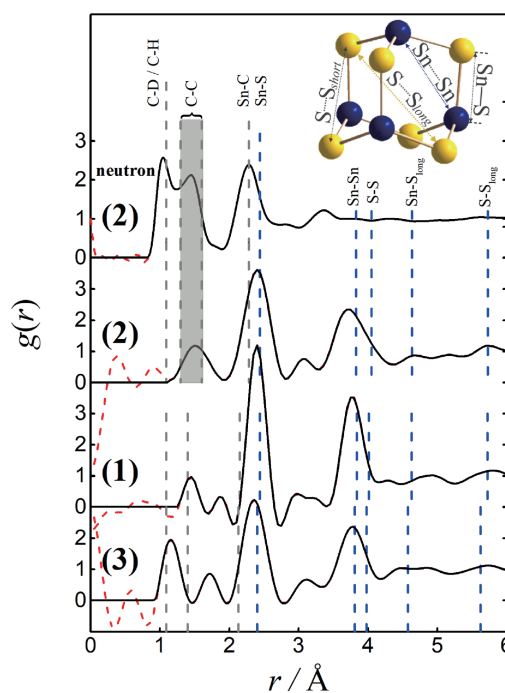
4. Results and Discussion

Total structure factors $S(Q)$, as obtained from X-ray scattering on **(1)**, **(2)**, and **(3)** are displayed in Fig. 3 as the lower three curves by the symbols. The neutron-based $S(Q)$ is shown as the upper curve, also displayed by symbols. Corresponding molecular formfactors $f_1(Q)$ were calculated according to Eq. (4) and are displayed by the lines. Structural data based on DFT calculations[13,14] were used for the computations. They confirm that the molecular structure is well reflected by in the experimental data for the amorphous solids, and that the basic structural motifs of heteroadamantane clusters can basically be confirmed for all of the materials. Special positions of the organic ligands which can freely rotate around the Sn–C axis in the free single molecules, were not considered in these calculations. They were used as suggested by the DFT calculations for minimum free energy. However, the difference to the real situation in the amorphous solid seems not to be particularly important for the X-ray based $S(Q)$s, due to the smaller weighting factors of the C–C, C–H, and H–H correlations. $S(Q)$s of the amorphous samples and $f_1(Q)$s therefore show clear similarities because both are mainly determined by the scattering from the molecular Sn–S core and not from the organic ligands. The most striking difference is a pronounced peak around $0.6\,Å^{-1}$ in the experimental data, which is not present in $f_1(Q)$. In this Q-range, the latter increases monotonically with vanishing momentum transfer and intersects the $S(Q)$ axis at a value given by the number of atoms in the molecule. The experimental $S(Q)$ peak, located around $0.6\,Å^{-1}$ in all of the X-ray $S(Q)$s thus represents a distinct intermolecular structural correlation. For the neutron-based $S(Q)$ of **(2)** however, the situation is clearly different. The coherent scattering lengths of C and D are now comparable with that of Sn and even more as twice as large
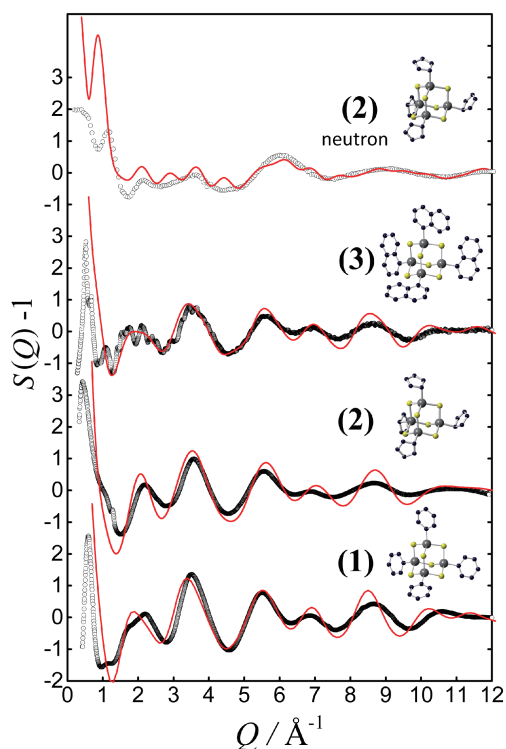
Fig. 3. (Color online) Symbols represent structure factors $S(Q)$ as obtained from X-ray scattering for molecules (**1**), (**2**), and (**3**), from bottom to top, respectively. The symbols of the upper data set represent the neutron $S(Q)$ from a deuterated sample of (**2**). Also shown as lines are the respective molecular formfactors as obtained from Eq. (4). For the neutron data of (**2**) a deuteration degree of 90% was estimated.

Fig. 4. (Color online) Total pair distribution functions $g(r)$ as obtained by Fourier transforming the $S(Q)$s of Fig. 3 for molecules (**1**), (**2**), and (**3**), respectively. The upper curve represents the neutron PDF of (**2**). Dashed vertical lines indicate atom–atom spacings in the DFT calculated molecules.[13,14] Dashed parts of $g(r)$ curves indicate the influence of truncation errors from Fourier transformation.

as that of S. Accordingly, the weighting factors of the C–C, C–D, D–D, and C–Sn correlations are larger than the Sn–S correlation. Hence, the cluster core does no longer dominate the scattering pattern. Therefore, the respective rotational orientation of the organic ligands plays an important role for the shape of $f_1(Q)$. The deviation from the real situation in the amorphous solid, which is unknown, is therefore now reflected by the difference between the structure factor and the molecular formfactor, especially in the lower Q-range. Here, an intense peak appears around $0.9\,\text{Å}^{-1}$ in $f_1(Q)$ which now however, is clearly intramolecular. This peak is also seen in $S(Q)$, however here, it is shifted to slightly larger Q at about $1.1\,\text{Å}^{-1}$.

Figure 4 shows the corresponding PDFs as obtained by Fourier-transformation of the experimental $S(Q)$s in Fig. 3. Five different interatomic distances exist within the Sn–S cluster core, as is illustrated by the inset in Fig. 4. The respective values as obtained from the DFT-calculated molecules are marked by vertical dashed lines. Also given as grey dashed lines are the values for the C–H, C–C, and the Sn–C chemical bonds.[13,14] It should however be noted, that the PDFs are subject to non-negligible truncation errors in the lower r-region, which we did not further address in our data reduction. The PDFs were set to zero below r-values of about $1\,\text{Å}$ which is close to the smallest physically reasonable value of the C–H bond. The truncation error influence is indicated by the dashed part of $g(r)$ in the lower r-range. For the X-ray PDFs the oscillations influence the pattern up to about $2\,\text{Å}$ where the contribution to $g(r)$ is weak since this is the range of the negligible C–H and C–C correlations. For the neutron

$g(r)$ of (**2**) these correlations have the largest weighting factors and these bonds are therefore prominently represented in the PDF. However, these correlations will not be further discussed in this report. For r-values above about $2\,\text{Å}$, $g(r)$ is determined mainly by correlations with heavy Sn atoms, so that the pattern there is determined by intense peaks that are only weakly influenced by the truncation problem. The Sn–C bond in (**2**) is longer than in the other two compounds. It is represented by a peak in the neutron-based $g(r)$ at $2.28\,\text{Å}$. For the X-ray-based PDFs this signal is slightly shifted to higher r ($2.35\,\text{Å}$) due to the larger weighting of the neighboring Sn–S correlation there. A further strong peak appears in all X-ray $g(r)$s at around $3.8\,\text{Å}$ comprising the Sn···Sn and S···S spacings. The Sn–Sn correlation possesses the dominating weighting for X-rays. However, its position at the high r side of this peak indicates that the Sn···Sn spacing may be smaller in the amorphous solids than in the calculated single molecules. For the WLGs (**1**) and (**2**) this shift seems to be slightly larger than for the SHG (**3**). Each Sn atom of the cluster core is also surrounded by three further S atoms which are located equally spaced around $4.6\,\text{Å}$ in the DFT-calculated molecules (Sn···S_{long}). For the amorphous SHG-material (**3**) a broad peak exists ranging from 4.3–$5.1\,\text{Å}$ and is centered around the DFT value. It is also visible in the $g(r)$s of the WLGs (**1**) and (**2**), but there it seems to be slightly shifted towards larger distances. Similarly, each sulfur is surrounded by four equally spaced sulfur neighbors (S···S) and one which sits further away at about $5.7\,\text{Å}$ (S···S_{long}). Broad peaks are here visible for the SHG material (**3**) and the two WLG materials (**1**) and (**2**), again shifted to slightly larger r values. The PDFs in Fig. 4 hence suggest that the lengths of the chemical bonds in the cluster core (Sn–
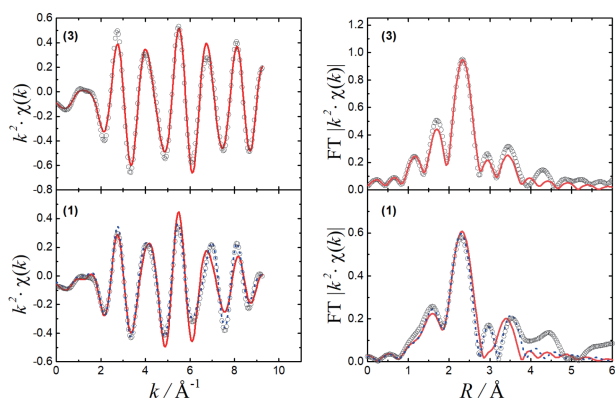
Fig. 5. (Color online) Experimental EXAFS data (symbols) for the amorphous materials (**1**) and (**3**), respectively (left-hand side), and corresponding Fourier transforms to R-space (right-hand side). Solid lines represent fits to the data using the DFT-calculated models. Dotted lines in spectra for (**1**) denote an extended fit using an additional scattering path to fit the data.

C and Sn–S) of the explored amorphous materials are similar to the respective values of the DFT-calculated clusters. However, nearest-neighbor distances spanning less than two bonds, like the Sn⋯Sn and S⋯S spacings, appear to be smaller than in their DFT-computed counterpart, while more distant spacings, spanning more than two bonds (Sn⋯S_{long} and S⋯S_{long}), are longer than calculated. This suggests that the cluster nuclei in the amorphous materials may be subject to some distortions and they appear to be slightly larger for the WLG materials than for the SHG material. This would define a clear difference between the two material classes. However, it is neither possible to make quantitative nor sustainable statements about such small effects only on basis of the total PDFs. Therefore, we have additionally carried out EXAFS studies on the amorphous WLG (**1**) and the amorphous SHG (**3**) to obtain more detailed structural information.[52] The corresponding data as obtained at the sulfur K-edge are displayed in Fig. 5 together with their real space Fourier-transforms.

The data were fitted using structural details from the DFT calculated molecules[13,14] as starting parameters. Both spectra can be fitted reasonably well (solid lines in Fig. 5). However, it is obvious that the fits for the SHG material (**3**) are considerably better than for the WLG material (**1**). This is a further hint that the molecular structure of the WLG-cluster experiences stronger modifications when being transferred into a dense amorphous phase as the SHG-cluster. The fit quality for the phenyl cluster (**1**) can however be improved by including an additional S–S or S–Sn fitting path at intermediate distance. This is shown in Fig. 5 by the dotted lines in the spectra for the phenyl cluster (**1**). Such an additional fitting path is indication that an additional atom is situated nearby either due to a distortion of the molecular structure or due to an additional intermolecular correlation. However, it must be stated, that the inclusion of this additional fitting path leads to a considerable dependence among the fitting parameters. Hence, additional constraints were needed to increase reliability of this procedure. To obtain further sustainable indications for the structural situation of the Sn–S cluster core, we have performed m-RMC simulations on the phenyl based WLG material (**1**)
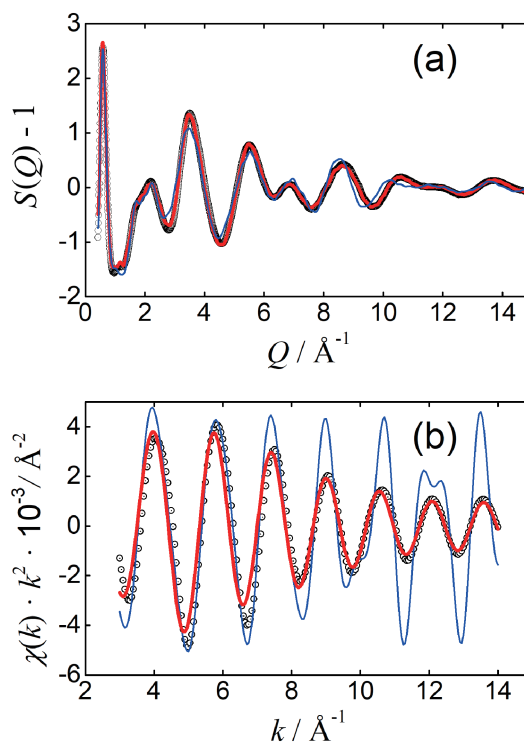

Fig. 6. (Color online) (a) Comparison between experimental (symbols) and dynamic m-RMC-simulated $S(Q)$ (thicker line) of (**1**). Thinner line represents simulation employing rigid molecular entities based on DFT-calculation.[13] (b) Comparison between experimental Sn K-edge EXAFS data (symbols) and m-RMC-simulation. Thinner line represents fit of rigid DFT-calculated clusters, thicker line shows the result of the dynamic simulation.

where X-ray diffraction and EXAFS data simultaneously served as constraints.[53] X-ray and Sn K-edge EXAFS data were both obtained from the PETRA III facility at DESY in Hamburg. They are depicted as symbols in Figs. 6(a) and 6(b), respectively. $S(Q)$ and EXAFS of a virtual ensemble of 216 molecules were iteratively computed during the simulation and should ideally converge towards the experimental curves. The thinner lines in Fig. 6 represent the outcome of the rigid-simulation attempt, where inflexible molecules of the DFT-calculated type were employed as molecular entities. It already reflects the essential details of the scattering pattern, but significant deviations still exist. In particular, a phase shift is visible, between the experimental and the simulated oscillations, which is especially pronounced between 8 and $12\,\text{Å}^{-1}$. Such a phase shift indicates that the real molecular structure in the amorphous solid deviates in shape and size from the DFT-calculated prediction. The differences between experiment and simulation are even more evident in the EXAFS data, where the simulation differs substantially from experiment also indicating that distances in the phenyl cluster (**1**) of the amorphous phase differ from the theoretical prediction. The result of the dynamic-simulation, where tin and sulfur atoms were allowed to vary their positions is depicted by the thicker lines in the two graphs. The atomic degrees of freedom unavoidably led to a variation of the molecular structure, but also to a rapid convergence of the simulations towards the experimental curves. The agreement with experiment is now excellent. Just small differences still remain at lower momentum transfer, possibly owed to the uncertainty of the exact carbon positions
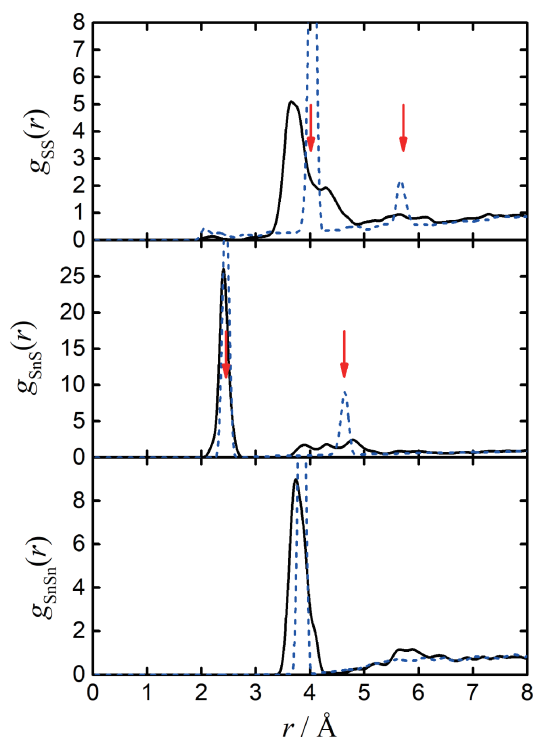
Fig. 7. (Color online) Partial PDFs $g_{SnSn}(r)$, $g_{SnS}(r)$, and $g_{SS}(r)$, as obtained from the dynamic RMC-simulation (solid black lines). Same functions are also shown, obtained from the rigid RMC-simulation (dashed lines).

Fig. 8. (Color online) $g_{SnS}(r)$ and $g_{SS}(r)$ of Fig. 7 further split into intra- and intermolecular contributions. Dashed vertical lines represent values for the DFT-calculated cluster core.[13] Solid lines give the integral values over the radial distribution functions, determining the number on neighbors as function of r.

due to their small weighting. The difference between thin and thick curves clearly shows that the rigid DFT-calculated molecule is in fact not a suitable model to reproduce the experimental data of the amorphous solid. The virtual molecular ensemble of the dynamic m-RMC simulation allows to extract partial PDFs for the Sn–Sn, Sn–S, and the S–S correlations. In turn, this allows direct access to the structural properties of the Sn–S cluster core in the amorphous solid. They are shown in Fig. 7. Dashed lines represent the partial PDFs of the rigid simulation, while the black solid lines give the PPDFs of the dynamic approach. Clear differences between the two data sets exist. For the rigid molecule, the PPDFs are entirely determined by the expected intramolecular distances of the core atoms which are marked by arrows for the Sn–S and S–S correlations. Distinct intermolecular correlations cannot be identified. E.g., for the Sn–Sn correlation, one only observes the atomic distance inside the Sn tetrahedron. Apart from that, the PPDF grows within the statistical error continuously towards one with increasing r, representing a pure stochastic probability of encountering intermolecular Sn atoms without any distinct correlation. The PPDFs of the dynamic simulation show a completely different picture: The Sn⋯Sn distance is slightly smaller than found in the DFT-calculation and the peak is slightly asymmetric, already indicating that the Sn$_4$ frame is subject to some distortion. Also, between about 5.5 and 6.2 Å, clear indication exists for intermolecular correlations. PPDFs containing sulfur correlations deviate even more significantly from the rigid molecule expectations. Except for the direct Sn–S bond, all other S⋯S and Sn⋯S distances seem to split into different spacings indicating strong deformation of the cluster core. We therefore further separated the PPDFs
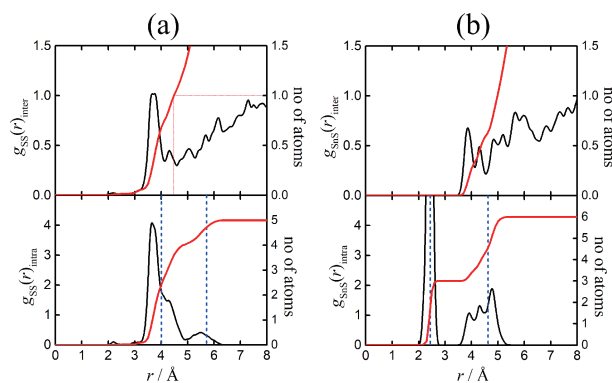
into inter- and intramolecular contributions which are shown in Fig. 8. The intramolecular contributions of the S–S and the Sn–S correlations are shown in the lower graphs of Figs. 8(a) and 8(b) which respectively represent the S–S and the Sn–S relations. The intermolecular PDFs are displayed in the upper graphs. The solid lines, belonging to the right-hand scales, represent the integrals over the respective partial radial distribution function (PRDF) $4\pi r^2 ng(r)$, with n being the neighboring atom density. This curve defines the number of neighboring atoms hidden under the PPDF peaks. In the rigid cluster core, every sulfur atom is surrounded by four identical neighbors located at 4.01 Å as is indicated by a dashed vertical line. In the amorphous solid these neighbors split into two groups, each containing two atoms, as indicated by the PRDF integral. One group is represented by a larger higher narrower peak at about 3.68 Å and the second by a smaller but broader peak at about 4.18 Å. Each sulfur atom of the rigid cluster also has a further well-defined, but more distant single sulfur neighbor at 5.72 Å, again indicated by a vertical dashed line. In the amorphous solid, this correlation is only visible as a broad peak situated between 5 and 6 Å with maximum slightly shifted to smaller distance.

The Sn atom of the rigid model cluster is chemically bonded to 3 sulfur atoms each at 2.44 Å but also by three identical neighbors, two bonds away, located 4.63 Å apart (Sn⋯S$_{long}$) as shown in the lower graph of Fig. 8(b) by the vertical lines. However, in the amorphous solid the latter correlation splits into three components situated between 3.5 and 5.5 Å, each containing one single atom. Again, the center of this group is shifted to values below the original rigid cluster value. The ensemble averages displayed in Figs. 7 and 8 clearly demonstrate, that the cluster cores in the amorphous [(PhSn$_4$)S$_6$] solid (**1**) are considerably deformed as compared to their counterparts computed with DFT methods. It is also obvious that it is the sulfur which is mainly responsible for these structural variations. Analyzing the atom–atom correlation between different molecules gives a similarly interesting picture. This is visualized by the upper graphs of Fig. 8. A pronounced correlation peak ranging from about 3 to 4.4 Å and centered at about 3.7 Å is found for the intermolecular S–S correlation which is depicted in Fig. 7(a). The corresponding PRDF-integral reveals one

atom, indicating that every cluster core of the RMC ensemble is on average surrounded by one S-atom of another cluster core on this length scale. It should be noted that such distances are well inside the range of intramolecular S···S spacings. The intermolecular Sn–Sn correlation in the upper plot of Fig. 8(b) shows a similar increase in the RPDF integral, but involves only about half an atom on a comparable length scale, indicating that it is the sulfur that imposes the dominant relationships between the molecules in the amorphous WLG solid.

In order to get more information on the relative spatial arrangement of different clusters from the dynamic computer ensemble, we have computed molecular centers of mass (MCMs) for each of the molecules and calculated the corresponding PDF of these centers, which is shown in Fig. 9. Distinct peaks are visible in the molecular PDF indicating that the molecular arrangement comprises clear intermolecular correlations. A first peak is centered at 7.5 Å and ranges from about 5.5 to 8 Å. This coincides exactly with values from a quantum chemical approach where dimers were considered as a minimal model for the amorphous system.[16] The integral over the corresponding RDF (solid line in Fig. 9, right scale) shows that each molecule is on average surrounded by two neighbors (dashed lines indicate the integration area). Another maximum appears between 10 and 14 Å, indicating that the molecules may arrange into chains. The inset in Fig. 9 illustrates the distribution of MCMs inside the simulation box. Bonds between molecules with distances between 5.5 and 8 Å were drawn to visualize the mutual spatial correlations of the clusters. In fact, it can be seen that chain-like structures of different lengths, partly branched, are indeed formed. A closer analysis shows, that about 20–25% of all clusters are bound in dimers with spacings between 6–7.5 Å.[53] The mutual arrangement of the phenyl clusters bound in such chain like structures is an alternating staggered configuration, where the ligands of one cluster are located in the voids between those of another cluster. As an example, Fig. 10 shows the arrangement of molecules in an arbitrarily chosen four atomic linear chain. Similar mutual molecular arrangements have already been predicted by the quantum chemical calculations.[16] Such an arrangement is also found in the crystalline compound **(4)** containing molecular building blocks very similar to those studied in our m-RMC exploration, where just Sn has been replaced by Si.[16] We thus find that the molecules are relatively strongly correlated and form superstructures of linear and partly branched chains. Thereby, their molecular centers of mass approach distances close to those predicted by theory for dimers.[16] Here, the spacings are, however, slightly larger which can be attributed to the fact that the interaction in the solid is shared by more than one neighbor. Moreover, the individual molecules are clearly distorted as compared to the respective DFT-calculated structures and these distortions result mainly from position changes of the sulfur atoms. It is noticeable that the overall difference between intra- and intermolecular S–S distances seems to disappear. Apparently, the sulfur atoms try to distribute themselves evenly over the sample, as far as this is possible despite their inclusion into the molecular adamantane frame-work. To illustrate this, some sulfur–sulfur distances are given for the four-molecule chain shown in Fig. 10 where
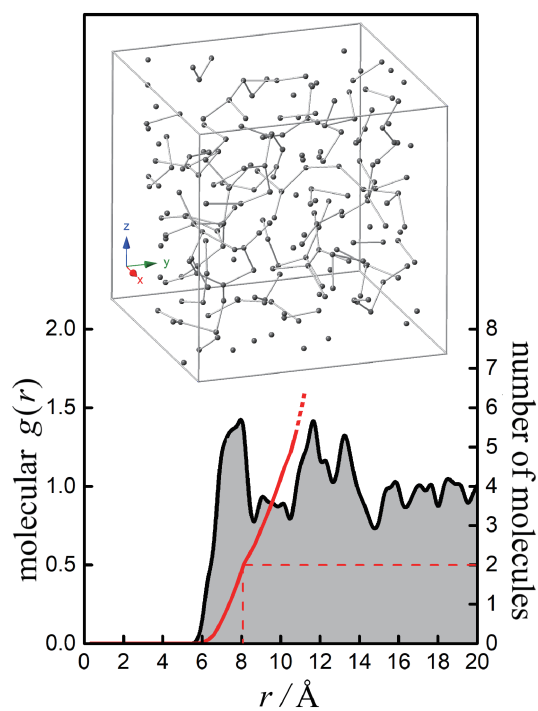
Fig. 9. (Color online) Molecular PDF, $g(r)$, as obtained from the MCMs of the dynamic simulation ensemble. Full line represents again the integral over the RDF to give the number of surrounding molecules. The inset shows MCMs from the dynamic simulation with bonds for spacings between 5.5 and 8 Å.
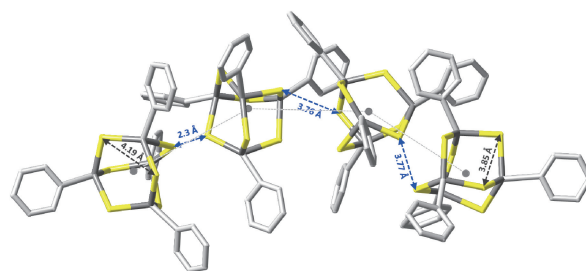
Fig. 10. (Color online) Fourfold linear chain, arbitrarily chosen out of the dynamic m-RMC simulation ensemble. H-atoms have been omitted to retain clarity. Molecules in chains prefer a staggered mutual configuration with respect to the organic ligands. MCMs are displayed by grey bullets connected by dashed lines. Also shown are some intramolecular and intermolecular distances, indicating similarity between intra- and intermolecular sulfur–sulfur spacings.

intramolecular and intermolecular distances are respectively depicted.

5. Conclusions

Two amorphous Sn–S based WLG materials with organic phenyl and cyclopentadienyl ligands, together with another amorphous Sn–S based SHG material containing naphthyl attached to the tin atoms, were explored using X-ray and neutron scattering, EXAFS and molecular RMC simulation to identify microscopic structural differences between the two material classes. Overall, the results indicate that the adamantane-like molecular building blocks in the WLG materials are subject to deformations that are not observed that way in the SHG material. Molecular RMC simulations performed for the phenyl-based WHG material suggest that

these distortions are mainly resulting from positional variations of the sulfur atoms. Moreover, it appears that the sulfur atoms in the amorphous WLG materials attempt to distribute as evenly as possible over the amorphous solid, and are only hindered by their molecular integration. It seems that more S···S$_{short}$ spacings are needed to reproduce the X-ray and EXAFS patterns than are actually present in the cluster cores. Therefore, intermolecular S···S spacings are employed, which, however, is only possible by appropriate deformation. In the real solid, this process may be driven by strong core–core interactions which were identified previously by theory.[16] These deformations also explain the high degree of isotropic interactions between the clusters reported there, which elsewhere was made responsible for the tendency to suppress crystallization.[53] The nearly uniform distribution of sulfur atoms resembles a close-meshed net, and since no chemical bonds exist between the sulfur atoms one may identify this as a vibrational network. Such a network would offer the option to generate a corresponding phonon-based atom dynamic which could then offer a wide range of k values to enable a broad receptivity for infrared radiation. Since such a scenario is exclusively restricted to disordered materials, it would explain why only amorphous Sn–S based materials show the WLG effect.

*pilgrim@staff.uni-marburg.de

1) S. Nakamura, T. Mukai, and M. Senoh, Appl. Phys. Lett. **64**, 1687 (1994).
2) C.-C. Yang, C.-M. Lin, Y.-J. Chen, Y.-T. Wu, S.-R. Chuang, R.-S. Liu, and S.-F. Hu, Appl. Phys. Lett. **90**, 123503 (2007).
3) C. C. Lin and R.-S. Liu, J. Phys. Chem. Lett. **2**, 1268 (2011).
4) N. C. George, K. A. Denault, and R. Seshadri, Annu. Rev. Mater. Res. **43**, 481 (2013).
5) M. Shang, C. Li, and J. Lin, Chem. Soc. Rev. **43**, 1372 (2014).
6) J. H. Burroughes, D. D. C. Bradley, A. R. Brown, R. N. Marks, K. Mackay, R. H. Friend, P. L. Burns, and A. B. Holmes, Nature **347**, 539 (1990).
7) M. A. Baldo, D. F. O'Brien, Y. You, A. Shoustikov, S. Sibley, M. E. Thompson, and S. R. Forrest, Nature **395**, 151 (1998).
8) T. Tsujimura, *OLED Display Fundamentals and Applications* (Wiley, Hoboken, NJ, 2017) Wiley Series in Display Technology, 2nd ed.
9) N. Thejokalyani and S. Dhoble, Renewable Sustainable Energy Rev. **32**, 448 (2014).
10) R. R. Alfano, *The Supercontinuum Laser Source* (Springer, New York, 2016).
11) J. M. Dudley, G. Genty, and S. Coen, Rev. Mod. Phys. **78**, 1135 (2006).
12) N. W. Rosemann, J. P. Eusner, A. Beyer, S. W. Koch, K. Volz, S. Dehnen, and S. Chatterjee, Science **352**, 1301 (2016).
13) N. W. Rosemann, J. P. Eusner, E. Dornsiepen, S. Chatterjee, and S. Dehnen, J. Am. Chem. Soc. **138**, 16224 (2016).
14) E. Dornsiepen, F. Dobener, S. Chatterjee, and S. Dehnen, Angew. Chem. **131**, 17197 (2019).
15) S. Dehnen, P. R. Schreiner, S. Chatterjee, K. Volz, N. W. Rosemann, W.-C. Pilgrim, D. Mollenhauer, and S. Sanna, ChemPhotoChem **5**, 1029 (2021).
16) K. Hanau, S. Schwan, M. R. Schafer, M. J. Muller, C. Dues, N. Rinn, S. Sanna, S. Chatterjee, D. Mollenhauer, and S. Dehnen, Angew. Chem. **133**, 1196 (2020).
17) W. Friedrich, Phys. Z. **14**, 317 (1913).
18) P. Debye and P. Scherrer, Nachr. Ges. Wiss. Gottingen, 1 (1916).
19) W. Friedrich, P. Knipping, and M. Laue, Ann. Phys. **346**, 971 (1913).
20) H. E. Fischer, A. C. Barnes, and P. S. Salmon, Rep. Prog. Phys. **69**, 233 (2006).
21) J. R. Stellhorn, S. Hosokawa, and W.-C. Pilgrim, Z. Phys. Chem. **228**, 1005 (2014).
22) T. E. Faber and J. M. Ziman, Philos. Mag. **11**, 153 (1965).
23) P. H. Fuoss, P. Eisenberger, W. K. Warburton, and A. Bienenstock, Phys. Rev. Lett. **46**, 1537 (1981).
24) K. F. Ludwig, W. K. Warburton, L. Wilson, and A. I. Bienenstock, J. Chem. Phys. **87**, 604 (1987).
25) Y. Waseda, S. Kang, K. Sugiyama, M. Kimura, and M. Saito, J. Phys.: Condens. Matter **12**, 195 (2000).
26) S. Hosokawa, J. R. Stellhorn, W.-C. Pilgrim, and J.-F. Berar, Z. Phys. Chem. **230**, 313 (2016).
27) J. Powles, Adv. Phys. **22**, 1 (1973).
28) R. L. McGreevy and M. A. Howe, Annu. Rev. Mater. Sci. **22**, 217 (1992).
29) R. McGreevy, Nucl. Instrum. Methods Phys. Res., Sect. A **354**, 1 (1995).
30) S. Hosokawa, W.-C. Pilgrim, J.-F. Berar, and P. Boolchand, J. Non-Cryst. Solids **431**, 31 (2016).
31) A. Zeidler, P. S. Salmon, D. A. J. Whittaker, A. Piarristeguy, A. Pradel, H. E. Fischer, C. J. Benmore, and O. Gulbiten, R. Soc. Open Sci. **5**, 171401 (2018).
32) P. S. Salmon, S. Xin, and H. E. Fischer, Phys. Rev. B **58**, 6115 (1998).
33) M. Howe, Mol. Phys. **69**, 161 (1990).
34) M. Scheidler, A. N. North, and J. C. Dore, Mol. Simul. **11**, 345 (1993).
35) R. L. McGreevy, J. Phys.: Condens. Matter **13**, R877 (2001).
36) A. K. Soper, Mol. Phys. **99**, 1503 (2001).
37) A. Nilsson and L. Pettersson, Chem. Phys. **389**, 1 (2011).
38) P. A. Bopp, J. B. Buhn, H. A. Maier, and M. J. Hampe, Chem. Eng. Commun. **195**, 1437 (2008).
39) E. R. Hernandez, L. M. M. Zetina, G. T. Vega, M. G. Rocha, L. F. R. Ochoa, and R. L. Fernandez, AIP Conf. Proc., 2008, p. 95.
40) J. J. Rehr, J. J. Kas, F. D. Vila, M. P. Prange, and K. Jorissen, Phys. Chem. Chem. Phys. **12**, 5503 (2010).
41) O. Bunau, A. Y. Ramos, and Y. Joly, International Tables for Crystallography I, 2021.
42) B. K. Teo, *EXAFS: Basic Principles and Data Analysis* (Springer, Berlin/Heidelberg, 1986).
43) B. Ravel and M. Newville, J. Synchrotron Radiat. **12**, 537 (2005).
44) J. J. Rehr and R. C. Albers, Rev. Mod. Phys. **72**, 621 (2000).
45) S. Calvin and K. E. Furst, *XAFS for Everyone* (CRC Press, Boca Raton, FL, 2013).
46) A.-C. Dippel, H.-P. Liermann, J. T. Delitz, P. Walter, H. Schulte-Schrepping, O. H. Seeck, and H. Franz, J. Synchrotron Radiat. **22**, 675 (2015).
47) J. Filik, A. W. Ashton, P. C. Y. Chang, P. A. Chater, S. J. Day, M. Drakopoulos, M. W. Gerring, M. L. Hart, O. V. Magdysyuk, S. Michalik, A. Smith, C. C. Tang, N. J. Terrill, M. T. Wharmby, and H. Wilhelm, J. Appl. Crystallogr. **50**, 959 (2017).
48) A. Polidori, R. F. Rowlands, A. Zeidler, M. Salanne, H. E. Fischer, B. Annighofer, S. Klotz, and P. S. Salmon, J. Chem. Phys. **155**, 194506 (2021).
49) O. Gereben and L. Pusztai, J. Comput. Chem. **33**, 2285 (2012).
50) B. D. Klee, E. Dornsiepen, J. R. Stellhorn, B. Paulus, S. Hosokawa, S. Dehnen, and W.-C. Pilgrim, Phys. Status Solidi B **255**, 1870138 (2018).
51) B. D. Klee, B. Paulus, S. Hosokawa, M. T. Wharmby, E. Dornsiepen, S. Dehnen, and W.-C. Pilgrim, J. Phys. Commun. **4**, 035004 (2020).
52) J. R. Stellhorn, S. Hayakawa, B. D. Klee, B. Paulus, J. Link Vasco, N. Rinn, I. Rojas Leon, S. Dehnen, and W.-C. Pilgrim, Phys. Status Solidi B, 2200088 (2022) [DOI: 10.1002/pssb.202200088].
53) B. D. Klee, B. Paulus, J. Link Vasco, S. Dehnen, S. Hosokawa, J. R. Stellhorn, S. Hayakawa, and W.-C. Pilgrim, arXiv:2204.03515.
54) B. D. Klee, G. J. Cuello, H. E. Fischer, B. Paulus, W.-C. Pilgrim, and A. Zeidler, Institute Laue–Langevin (ILL), 2020 [DOI: 10.5291/ILL-DATA.6-05-1019].

Wolf-Christian Pilgrim obtained his diploma and doctoral degree in Physical Chemistry in 1988 and 1992 from the Philipps-University of Marburg. After a postdoctoral Humboldt fellowship in Solid State Physics at the Oregon-State University (1993–1995) he completed his Habilitation in Physical Chemistry in 2000. Since 2005 he is Professor for Physical Chemistry at the Philipps-University in Marburg. His research focuses on structure and dynamics in liquids and disordered solids and matter under extreme conditions of pressure and temperature using X-ray and neutron scattering techniques.

Jens Rüdiger Stellhorn received his Ph.D. in Chemistry from the Philipps-University Marburg (Germany). He has since worked as postdoctoral researcher at the Nagoya Institute of Technology, Kumamoto University (both Japan) and at the DESY synchrotron in Hamburg (Germany). Since 2019, he is working as assistant professor in the department of Applied Chemistry at Hiroshima University (Japan). His main research interests concern the advanced atomic-scale characterization of complex systems, and the relationship of the structure with physical properties, in particular using methods available at large-scale research facilities.

Benjamin D. Klee was born in Marburg, Germany in 1988. He studied chemistry at the Philipps-University in Marburg where he received his doctoral degree in 2020. After finishing a postdoctoral project in Marburg, he joined the Wigner Research Institute for Physics in Budapest, Hungary in 2022. His research work mainly includes the application of scattering techniques to non-crystalline systems and structure determination using Reverse-Monte-Carlo modeling.

Jonathan Link Vasco was born in Guayaquil, Ecuador in 1992. He obtained his master's degree in chemistry at the Philipps-University in Marburg in 2020 and is currently doing his Ph.D. at the research group of Professor Wolf-Christian Pilgrim. His research focuses on scattering techniques of disordered solids and structure modeling using the Empirical Potential Structure Refinement and Reverse-Monte-Carlo computer simulation programs.

Benedict Paulus studied Chemistry in Marburg, Germany and obtained his M.Sc. degree in 2017. Since then he is working on his Ph.D. in Marburg under supervision of Professor Wolf-Christian Pilgrim about the structure of amorphous phase change materials. His research is based on scattering methods using x-rays and neutrons.

Anita Zeidler graduated in Chemistry at the Philipps-University of Marburg/Germany in 2004 before receiving her PhD in Physics from the University of Bath/UK in 2009. She subsequently worked as a Postdoc before receiving a 5-year Royal Society - EPSRC Dorothy Hodgkin Research Fellowship in 2015. Since 2017 she is a lecturer at the University of Bath. Her interest is in amorphous materials (liquids, glasses, disordered crystals) and the relation of their properties with the atomic scale structure at ambient and extreme conditions of high pressures and temperatures.

Shinya Hosokawa was born in Kagawa, Japan in 1955. He obtained his Ph.D. from Kyoto University in 1986. He was an assistant professor at Hiroshima University from 1985, and an associate professor from 1991. He was a Humboldt fellow from 1995, and senior scientist at University of Marburg in Germany from 1997. He was an associate professor at Hiroshima Institute of Technology in 2004. From 2012 to 2021, he was a professor at Kumamoto University, and currently a project professor at Institute of Industrial Nanomaterials, Kumamoto University, Japan. He has worked on experimental studies of structure and dynamics on non-crystalline materials by using synchrotron radiation.

Shinjiro Hayakawa received his Ph.D. in Applied Chemistry from the University of Tokyo (Japan) in 1991. He was an assistant professor at the University of Tokyo from 1991 to 1999, and moved to Hiroshima University as an associate professor in 1999. Since 2014 he is a professor at Hiroshima University. He has been working with X-ray fluorescence spectroscopy and X-ray absorption spectroscopy and their applications to materials science.

Stefanie Dehnen obtained her diploma in 1993 and her doctoral degree in 1996 from the University of Karlsruhe (KIT). After a postdoctoral stay in theoretical chemistry (1997) she completed her Habilitation in inorganic chemistry in 2004. As of 2006 she has been Full Professor of Inorganic Chemistry at Philipps-Universität Marburg. She is a full member of the European Academy of Sciences (EurASc) and of Leopoldina German National Academy of Sciences and awardee of the 2022 Leibniz Prize from the German Research Foundation (DFG). Her current research is focused on the synthesis and experimental as well as quantum chemical investigation of compounds with multinary, in particular multimetallic, molecular nano-architectures, which possess potential as innovative catalysts, white-light emitters, or battery materials.